Centromere instability links genome damage to immune activation in systemic sclerosis

Azait Imtiaz[1], Mohammad Waseem[1], Hudson O'Neill[1], Bo-Ruei Chen[2], Wioletta Czaja[1], Rafael Contreras-Galindo[1*]

[1]Department of Genetics, University of Alabama at Birmingham, Birmingham, Alabama, 35233, USA
[2]Department of Pediatrics, Washington University in St. Louis, MO, 63001, USA.

* To whom correspondence should be addressed to:
Rafael Contreras-Galindo
Assistant Professor
Department of Genetics
University of Alabama at Birmingham
McCallum 627, 1918 University Blvd,
Birmingham, Alabama, 35233, USA
Email : contrerr@uab.edu
Phone : 205-934-5187

Abstract

Systemic sclerosis (SSc) is a fibrotic autoimmune disease in which genomic sources of instability and their immunological consequences remain poorly defined. We show that bleomycin, a widely used SSc fibrosis model, induces DNA double-strand breaks (DSBs) at active centromeres. Comparable centromeric damage was detected in fibroblasts from patients with limited cutaneous SSc, affecting nearly half of cells. Quantification of α-satellite repeat length revealed deletions and insertions, paralleling alterations observed in diffuse and limited SSc. These breaks are repaired primarily by ATM-dependent RAD51-mediated homologous recombination, but repair remains incomplete. Unresolved lesions disrupt kinetochore assembly, promote chromosome missegregation, and generate micronuclei and cytoplasmic chromatin enriched in centromere proteins. These fragments escape via nuclear envelope rupture, colocalize with MHC class II molecules, and may provide a potential mechanistic basis for anti-centromere antibody generation. Together, these findings establish centromere instability as a unifying driver of chromosomal instability, immune activation, and fibrosis in SSc, providing a mechanistic link between genome instability and autoimmunity.

Keywords: Systemic Sclerosis, Alpha-satellite DNA, DNA double-stranded breaks, Bleomycin, Micronuclei

Introduction

Systemic sclerosis (SSc), or scleroderma, is a chronic autoimmune disease characterized by vascular injury, immune dysregulation, and progressive fibrosis of the skin and internal organs [1–4]. A defining clinical feature of limited cutaneous SSc (lcSSc) is the presence of anti-centromere antibodies (ACAs), directed against centromeric proteins such as CENP-A and CENP-B [5,6]. Yet the origin of these autoantigens remains unexplained. While recent progress has clarified immune pathways that sustain fibrosis [7–11], far less is known about how centromere fragility contributes to chromosomal instability and autoantigen generation [2,12].

Human centromeres are composed of ~171-bp α-satellite monomers arranged into higher-order repeat (HOR) arrays . These AT-rich repeats, of which only a subset harbor CENP-B boxes, are packaged into specialized chromatin marked by CENP-A [13,14]. Array size and organization vary extensively across individuals, with up to 30-fold differences recently revealed by near-complete genome assemblies [15]. While centromeres are essential for accurate chromosome segregation, their repetitive nature, secondary structure features and chromatin context make them prone to replication stress and DNA damage [16–20]. Damage within α-satellites disrupts kinetochore assembly and drives chromosomal instability (CIN), manifested by aneuploidy and micronucleus formation [17,21–23]. Mis-segregated chromosomes frequently form micronuclei that undergo rupture, releasing DNA into the cytoplasm. Cytosolic DNA can activate innate immune sensors such as cGAS, inducing interferon responses [2,24–26], and can associate with HLA class II molecules, including alleles linked to autoimmunity, thereby facilitating neoantigen presentation [27–30]. These processes offer a plausible mechanism for ACA production in lcSSc but have not been mechanistically linked to centromere instability.

Bleomycin (BLM), a chemotherapeutic antibiotic and widely used experimental fibrosis inducer, generates reactive oxygen species that produce both single- and double-strand DNA breaks (DSBs) [31,32]. Early studies demonstrated preferential BLM cleavage within repetitive DNA, including α-satellite sequences [33–36]. In vivo, BLM administration recapitulates key features of SSc, including dermal fibrosis, fibroblast activation, and extracellular matrix accumulation [37–39]. These properties make BLM a powerful model to test whether centromeric DNA damage drives CIN, immune activation, and autoantibody generation in SSc [2,40]. However, the repair dynamics of centromeric DSBs remain poorly understood. DSBs can be resolved by non-homologous end joining (NHEJ) or homologous recombination (HR), but in repetitive DNA, misalignment during HR can lead to deletions or insertions [41–43]. While CENP-A accumulation has been reported at induced damage sites [44,45], it is unclear whether this reflects recruitment of repair factors or the intrinsic fragility of centromeric chromatin.

Here, we use BLM-induced DNA damage in fibroblasts and in vivo skin fibrosis models to investigate centromere fragility in the context of SSc. Through α-satellite qPCR, immunofluorescence mapping, ATM inhibition, and patient fibroblast analyses, we demonstrate that BLM induces DSBs at active centromeres. These lesions are repaired primarily by RAD51-mediated HR but remain unstable, resulting in DNA loss, kinetochore disruption, missegregation, and micronucleus formation. Damaged centromere chromatin escapes into the cytoplasm through nuclear envelope rupture, where it colocalizes with HLA-DRB1. Together, these findings establish centromere instability as a likely contributor to CIN and immune activation in SSc, linking genotoxic injury to autoantigen exposure and fibrosis.

Results

Centromere instability in BLM-induced scleroderma fibrosis models

To test whether BLM induces centromere instability in a fibrosis-relevant context, we first used the intradermal BLM mouse skin model, which reproduces dermal thickening, collagen deposition, and fibroblast activation. Mice received BLM injections every other day for 14 days. By day 14, fibrotic skin showed marked dermal thickness, erythema, and hydroxyproline compared with vehicle controls (Fig. 1A–D). Quantitative PCR (qPCR) of centromeric repeats revealed significant copy number loss, with deletions of ~50% for MaSat, ~60% for MiSat, and ~70% for Ymin in fibrotic tissue (Fig. 1E).

In human fibroblasts (CHON-002), BLM exposure (1.7–7.0 μM, 1–3 h) caused a rapid reduction in α-satellite DNA at 2 h, followed by partial recovery at 3 h, consistent with ongoing repair (Fig. 1F). At higher doses (7.0 μM), instability persisted. After 24 h recovery, qPCR showed sustained copy number alterations (predominately deletions, with occasional insertions) across multiple α-satellite arrays, including ~50% deletions at several centromere arrays (D1Z5, D6Z1, D15Z3, D18Z1) (Fig. 1G). BJ-5ta fibroblasts displayed a similar pattern but the extent of centromere alterations was more severe, with deletions and insertions occurring at comparable frequency, and persistent losses at D5Z1, D7Z1, D9Z4, and D17Z1 (Supplementary Fig. 1A–B).

MTT assays confirmed ~75–80% viability at 3.5–7.0 μM (Supplementary Fig. 2), indicating that centromere copy number changes reflect targeted genomic instability rather than nonspecific cytotoxicity.

BLM-induced double-strand breaks at active centromeres

We next asked whether BLM preferentially induces DSBs at centromeres marked by CENP-A. CHON-002 fibroblasts treated with 3.5 or 7.0 μM BLM for 3 h showed strong γ-H2AX staining compared with untreated controls, consistent with widespread DSB induction (Fig. 2A). Similar results were obtained in BJ-5ta fibroblasts (Supplementary Fig. 3A), and western blotting confirmed increased γ-H2AX levels following BLM exposure (Supplementary Fig. 3B).

Colocalization analysis revealed that γ-H2AX foci frequently overlapped with centromeric markers. While CENP-A and CENP-B signals remained tightly correlated ($r > 0.85$) under all conditions, γ-H2AX colocalized more strongly with CENP-A ($r = 0.51–0.74$) than with CENP-B ($r = 0.31–0.50$), indicating preferential damage at active centromeres (Supplementary Fig. 3C–D).

To assess disease relevance, we examined fibroblasts from three SSc patients. γ-H2AX activation was observed in all samples. In fibroblasts from two lcSSc patients, γ-H2AX colocalized with CENP-A in ~50% of cells (Pearson's $r = 0.29–0.42$), compared with lower colocalization with CENP-B ($r = 0.09–0.19$). In contrast, fibroblasts from one dcSSc patient displayed γ-H2AX foci without significant CENP-A colocalization (<1% of cells; Fig. 2B, Supplementary Fig. 3E).

Together with the BLM experiments, these findings suggest that acute fibroblast models and patient-derived fibroblasts capture complementary aspects of centromere instability. In lcSSc, a subset of fibroblasts shows active colocalization of γ-H2AX with CENP-A, consistent with ongoing centromere fragility, whereas dcSSc fibroblasts primarily display evidence of prior centromere disruption without detectable ongoing DSB activity.

BLM-induced centromeric breaks are preferentially repaired by HR

To determine the DNA repair pathways engaged at centromeric DSBs, CHON-002 fibroblasts were treated with 3.5 or 7.0 μM BLM and immunostained for γ-H2AX (DSB marker), RAD51 (HR), and KU70 (NHEJ). Untreated cells showed minimal nuclear staining (Fig. 3A). BLM exposure induced robust γ-H2AX foci accompanied by strong RAD51 recruitment, while KU70 staining was weak and rarely overlapped with γ-H2AX.

Quantitative colocalization confirmed HR dominance. At 3.5 μM BLM, RAD51–γ-H2AX correlation was high ($r = 0.875$), compared with lower values for KU70–γ-H2AX ($r = 0.314$). At 7.0 μM, RAD51–γ-H2AX correlation further increased ($r = 0.919$), whereas KU70 associations remained low ($r = 0.276$) (Supplementary Fig. 4A). Gene expression analysis showed that RAD51 mRNA increased in a dose-dependent manner (****$p < 0.0001$), while KU70 showed only a modest but significant rise (**$p < 0.001$, Supplementary Fig. 4B). Kinetic analyses revealed temporal differences in repair factor localization. At 3 h post-treatment, RAD51 staining was diffuse, but by 24 h distinct RAD51 foci colocalized with γ-H2AX (Fig. 3A–B).

BLM activates PARP-dependent single-strand break and replication stress signaling

To assess the single-strand break (SSB) and replication stress response, we monitored poly(ADP-ribose) (PAR) polymer accumulation, a rapid marker of PARP activation. In untreated CHON-002 fibroblasts, PAR immunofluorescence was minimal or absent (Supplementary Fig. 4C). Exposure to 7.0 μM BLM induced robust nuclear PAR staining in ~20% of cells, where the signal was pan-nuclear and diffuse, consistent with transient global PARP activation during acute DNA damage. The remaining cells showed low or undetectable PAR signal, reflecting the rapid turnover of PAR polymers. Quantification confirmed a significant increase in nuclear PAR

intensity compared with untreated controls (****$p < 0.0001$, $n = 50$ cells) (Supplementary Fig. 4D). Although PAR staining indicated an SSB response, the predominant outcome of BLM exposure was DSB formation, as reflected by widespread γ-H2AX accumulation.

ATM-mediated phosphorylation is required for γ-H2AX and RAD51 recruitment to centromeric DSBs

ATM kinase phosphorylates H2AX to generate γ-H2AX at sites of DNA damage. To test whether ATM mediates BLM-induced centromeric signaling, CHON-002 fibroblasts were treated with 3.5 or 7.0 μM BLM for 3 h, with or without the ATM inhibitor KU-55933 (35 μM, 1 h pretreatment). BLM induced robust, dose-dependent accumulation of γ-H2AX foci, many colocalizing with the centromeric marker CENP-A (Fig. 4A). ATM inhibition markedly reduced γ-H2AX intensity at both doses, while CENP-A localization remained intact (Fig. 4A-C). Furthermore, ATM inhibition reduced RAD51 puncta accumulation, consistent with ATM-dependent RAD51 activation (Fig. 4D).

Quantitative analysis confirmed that γ-H2AX and RAD51 induction by BLM was almost completely suppressed by ATM inhibition (***$p < 0.001$, ****$p < 0.0001$, one-way ANOVA) (Fig. 4B,E). In contrast, CENP-A fluorescence levels were unaffected (Fig. 4C, ns). These findings indicate that ATM is the primary kinase required for γ-H2AX signaling and HR engagement at centromeric breaks, while CENP-A remains a centromere marker but is not directly involved in ATM-dependent repair.

BLM-induced DNA damage triggers micronuclei formation and centromere chromatin release

DAPI staining revealed a dose-dependent increase in micronuclei in CHON-002 fibroblasts treated with 3.5 or 7.0 μM BLM, whereas untreated controls were essentially free of micronuclei (Fig. 5A–B). Many micronuclei contained centromeric signals (Fig. 5C, Supplementary Fig. 5E), consistent with observations in SSc fibroblasts [2]. In untreated cells, CENP-A and CENP-B were localized exclusively to nuclear centromeres, consistent with patterns in healthy skin fibroblasts [2]. After BLM exposure, centromere chromatin was detected in the cytoplasm. At 7.0 μM, ~12% of cells displayed cytoplasmic centromere chromatin (****$p < 0.0001$, $n = 3$) (Fig. 5D), a finding confirmed in BJ-5ta fibroblasts (Supplementary Fig. 5A–D). Cytoplasmic DNA was detected in ~15% of cells at this dose (****$p < 0.0001$, $n = 3$), reinforcing that BLM promotes centromere chromatin leakage into the cytoplasm.

To test whether nuclear envelope rupture mediates this release, we examined BANF1, a marker of nuclear envelope stress/rupture. BANF1 was minimally detected in control cells but strongly accumulated at rupture sites on nuclei and micronuclei in BLM-treated fibroblasts (white arrows, Fig. 5E). Quantification confirmed significantly elevated BANF1 intensity (****$p < 0.0001$, $n = 10$) (Fig. 5F).

Patient fibroblasts showed similar phenotypes [2]. Consistently, lcSSc fibroblasts frequently displayed cytoplasmic centromeric chromatin, whereas dcSSc fibroblasts rarely did (Fig. 5G). This pattern is consistent with the higher prevalence of ACAs among lcSSc patients. In our prior analyses, ACAs were detected in 100% of patients with cytoplasmic centromere chromatin. Together with BANF1 redistribution, these findings implicate nuclear envelope rupture as a mechanism contributing to centromere chromatin release in lcSSc fibroblasts.

Centromere damage drives cytoplasmic mislocalization and MHC class II presentation

BLM-induced release of centromeric chromatin into the cytoplasm was observed in treated fibroblasts, consistent with prior reports in lcSSc [2]. To test whether BLM-induced centromere damage leads to immune presentation, we performed IF for CENP-B and HLA-DRB1. Treated fibroblasts showed robust cytoplasmic colocalization of CENP-B with HLA-DRB1, which was absent in untreated controls (Fig. 6). Colocalization was restricted to cells that exhibited cytoplasmic centromeric chromatin. Fibroblasts from ACA-positive lcSSc patients displayed strong colocalization, whereas cells without cytoplasmic centromere chromatin resembled the pattern seen in dcSSc [2]. These findings indicate that centromere damage can result in cytoplasmic mislocalization of CENP-B with MHC class II components, with heterogeneity across patient-derived fibroblasts.

Discussion

This study identifies centromeric DNA as a critical target of genotoxic stress in SSc. We demonstrate that BLM-induced breaks within centromeric α-satellite arrays are signaled through ATM-dependent γ-H2AX and repaired by RAD51-mediated HR, but lesions remain incompletely resolved, producing deletions or abnormal insertions in α-satellite DNA. A key consequence is the release of centromeric chromatin into the cytoplasm, where it colocalizes with MHC class II molecules and may provide a direct source of anti-centromere autoantigens. Parallel findings in patient fibroblasts and in the BLM-induced skin fibrosis model establish centromere instability as a disease-relevant driver of immune activation and fibrosis.

Centromeric repeats are intrinsically fragile due to their repetitive sequence composition, replication challenges, and specialized chromatin environment. Prior studies have shown that centromeres accumulate spontaneous lesions during both proliferation and quiescence, most often repaired through RAD51-mediated HR [18,20,46]. In our study, BLM markedly amplified this baseline fragility, producing deletions and insertions within α-satellite arrays. Alterations were more pronounced in BJ-5ta fibroblasts than in CHON-002 cells, suggesting that chromatin state or repair capacity influences centromeric vulnerability. The BLM-induced skin fibrosis model recapitulated these effects in vivo, showing consistent reductions in mouse centromeric satellites within fibrotic tissue. These findings are consistent with the known susceptibility of repetitive DNA, including α-satellites, to BLM-induced cleavage [32–35]. Thus, centromeric instability extends from cell culture to tissue-level fibrosis, consistent with reports of widespread centromere loss in SSc skin [2].

γ-H2AX foci colocalized with CENP-A, and ATM inhibition suppressed this response, demonstrating that centromeric lesions engage ATM-dependent signaling. Recruitment of RAD51, but not KU70, indicated preferential HR repair, although HR failed to fully restore array integrity. This is consistent with prior observations that clustered lesions or under-replicated centromeric DNA are often inaccurately repaired [20,46,47].

Functionally, centromere instability produced chromosome missegregation, micronuclei, and nuclear envelope rupture, marked by BANF1 redistribution and cytoplasmic release of centromeric chromatin. These cytoplasmic structures were present in ~12–15% of treated fibroblasts and mirrored phenotypes observed in SSc fibroblasts, particularly from patients with lcSSc. Cytoplasmic CENP-B colocalized with HLA-DRB1, implicating centromere fragments as substrates for MHC class II presentation and ACA generation. These findings extend established links between cytosolic DNA, cGAS-STING activation, and fibrosis by identifying centromeric DNA as a specific contributor to the cytosolic DNA pool [2,5,48–51].

In contrast to lcSSc, dcSSc fibroblasts displayed broader DNA damage and deeper centromeric deletions without sustained γ-H2AX/CENP-A colocalization. This distinction mirrors clinical observations: ACA predominance in lcSSc versus other autoantibodies and more severe fibrosis in dcSSc. The convergence of centromere instability, ACA generation, and HLA class II associations highlights subset-specific disease mechanisms [5,27,28].

This study has limitations. Fibroblast cultures and the BLM model may not fully capture the complexity of stromal–immune interactions in vivo, and direct demonstration of centromeric peptide processing and T-cell activation remains an important next step.

By positioning centromere instability at the intersection of chromosome instability, innate sensing, and autoantigen presentation, our findings provide a unifying framework that links

genome instability to immune activation in SSc. Similar mechanisms may underlie other autoimmune and fibrotic diseases where repetitive DNA is destabilized. Future work should test whether modulating DNA repair fidelity or directly targeting cGAS-STING can mitigate fibrosis arising from centromeric fragility. [52-55]

Methods

Reagents

Bleomycin sulfate (Cayman Chemical, Cat. No. 13877, Lot #0701763-49) was used in all experiments for consistency across experiments. All other reagents were of analytical grade and obtained from commercial suppliers unless otherwise noted.

Cell culture and treatments

hTERT-immortalized human fibroblasts (CHON-002, ATCC CRL-2847; BJ-5ta, ATCC CRL-4001) were cultured in Dulbecco's Modified Eagle Medium (DMEM; Gibco) supplemented with 10% fetal bovine serum (FBS; Gibco) and 1% penicillin–streptomycin (Gibco). Cells were maintained at 37 °C in a humidified incubator with 5% CO_2 and routinely tested for mycoplasma contamination.

For acute bleomycin (BLM) exposure, fibroblasts were seeded at 5×10^5 cells per well in 6-well plates and grown to 60–80% confluence. Cells were treated with 0, 3.5, or 7 μM BLM for 3 h. For recovery assays, cells were washed with phosphate-buffered saline (PBS) and incubated in drug-free medium for 24 h. For ATM inhibition, cells were pretreated with KU-55933 (35 μM, Selleck Cat. S1092) for 1 h prior to BLM treatment.

Mouse BLM-induced skin fibrosis model

C57BL/6 mice (Jackson Laboratory; 20–25 g; 2 males, 3 females per group) were randomized to receive intradermal injections of BLM (1 U/mL, 100 μL) or vehicle (PBS) into shaved dorsal skin every other day for 14 days. On day 14, mice were anesthetized with isoflurane (1-2%) and euthanized by cervical dislocation. Skin samples were collected from: (1) PBS-injected control sites, (2) adjacent uninjected skin, and (3) fibrotic BLM-injected lesions. Genomic DNA

was isolated for qPCR analysis. All animal studies were approved by the University of Alabama at Birmingham Institutional Animal Care and Use Committee (protocol 23172).

Human samples

Primary dermal fibroblasts were derived from patients with SSc under University of Michigan IRB HUM00065044, as previously described [2]. Cell lines were obtained from patients with limited cutaneous SSc (lcSSc) and diffuse cutaneous SSc (dcSSc), as well as from healthy controls.

DNA and RNA isolation

Genomic DNA was extracted using the Monarch Genomic DNA Purification Kit (NEB 30102) with RNase A treatment. Total RNA was isolated using the Direct-zol RNA MicroPrep Kit (Zymo Research) with on-column DNase digestion. Concentrations were measured with a Qubit 4 Fluorometer (Thermo Fisher). DNA and RNA were stored at −80 °C until use.

Centromere qPCR

Mouse centromeric arrays (MaSat, MiSat, and Ymin) were quantified by qPCR using validated primer sets [56]. Human α-satellite arrays (D1–D22, X, Y) were quantified using primer sets described previously [57]. Reactions were run on QuantStudio 3 (Applied Biosystems) with Radiant SYBR Green Master Mix (Alkali Scientific). Relative copy number was normalized to 18S, GAPDH, or TOP3A using the ΔΔCt method. Primer specificity was confirmed by melt-curve analysis.

Western blotting

Cells were lysed in RIPA buffer (ChemCruz) supplemented with protease and phosphatase inhibitors (Thermo Fisher). Lysates (20–30 µg protein) were resolved by SDS–PAGE (10%) and transferred to PVDF membranes (Bio-Rad). Membranes were blocked in 5% milk/TBST, incubated overnight at 4 °C with primary antibodies (Supplementary Table 1), and probed with HRP-conjugated secondary antibodies (2 h, room temperature). Signals were developed using Clarity ECL substrate (Bio-Rad) and imaged with a ChemiDoc MP system.

Immunofluorescence microscopy

Cells were fixed in 4% paraformaldehyde (PFA), permeabilized with PBST (0.2% Triton X-100), and blocked in 2% BSA/PBST. Coverslips were incubated with primary antibodies (Supplementary Table 1) for 1 h at 37 °C, followed by Alexa Fluor–conjugated secondary antibodies (1:1000, 45 min, room temperature). Nuclei were counterstained with DAPI (ProLong Gold, Thermo Fisher).

For chromosome spreads, cells were arrested with 10 µg/mL colcemid for 16 h, incubated in 0.075 M KCl for 15 min, cytospun at 290 × g for 5 min, and fixed in 4% PFA prior to IF staining. Images were acquired on an Olympus BX73 fluorescence microscope.

Quantitative RT-PCR

mRNA expression of RAD51 and KU70 was measured using the Luna One-Step RT-qPCR Kit (NEB) with 50 ng RNA per reaction on a QuantStudio 3 instrument. GAPDH was used as a reference gene, and relative expression was calculated using the ΔΔCt method. Primer sequences were obtained from published sources [58,59].

Statistical analysis

All qPCR experiments were performed in three independent biological replicates with technical duplicates. Immunofluorescence analyses were based on ≥50 randomly selected fields per condition. Western blotting was performed in at least three independent replicates. Statistical significance was determined by unpaired Student's t-test or one-way ANOVA with Tukey's or Dunnett's post hoc test, as appropriate (GraphPad Prism v9.3.1). A threshold of $p < 0.05$ was considered significant. Colocalization coefficients were calculated using the Coloc2 plugin in Fiji.

Data availability

The data generated in this study are provided in the Source Data file. Source data are provided with this paper.

Acknowledgements

We thank Dr. Arko Sen for insightful discussions. The authors thanked the National Scleroderma Foundation for supporting this project. R.C.-G. is the recipient of the Marta Marx Award for the Eradication of Scleroderma from the National Scleroderma Foundation.

Author contributions

R.C-G. and A.I. conceived and designed the study. R.C-G., A.I. and M.W. designed and performed the investigation. R.C-G acquired the funding. R.C-G., M.W., B.C., and W.C supervised the study. R.C-G., M.W., H.O., B.C., and W.C. wrote, reviewed and edited the manuscript.

Competing interest

Authors declare no competing of interest.

Additional information

Supplementary Information is available for this paper.

Funding

Startup funds from the University of Alabama at Birmingham, and the National Scleroderma Foundation supported R.C-G.

References

1. Volkmann, E.R., Andréasson, K. & Smith, V. Systemic sclerosis. *Lancet* **401**, 304–318 (2023).
2. Paul, S. et al. Centromere defects, chromosome instability, and cGAS-STING activation in systemic sclerosis. *Nat. Commun.* **13**, 7074 (2022).
3. van Bon, L., Cossu, M. & Radstake, T.R. An update on an immune system that goes awry in systemic sclerosis. *Curr. Opin. Rheumatol.* **23**, 505–510 (2011).
4. Rosendahl, A.H., Schönborn, K. & Krieg, T. Pathophysiology of systemic sclerosis (scleroderma). *Kaohsiung J. Med. Sci.* **38**, 187–195 (2022).
5. Kuwana, M. et al. HLA class II genes associated with anticentromere antibody in systemic sclerosis (scleroderma). *Ann. Rheum. Dis.* **54**, 983–987 (1995).
6. Akbarali, Y. et al. Fine specificity mapping of autoantigens targeted by anti-centromere autoantibodies. *J. Autoimmun.* **27**, 272–280 (2006).
7. Brown, M. & O'Reilly, S. The immunopathogenesis of fibrosis in systemic sclerosis. *Clin. Exp. Immunol.* **195**, 310–321 (2019).
8. Wei, J. et al. Fibrosis in systemic sclerosis: emerging concepts and implications for targeted therapy. *Autoimmun. Rev.* **10**, 267–275 (2011).
9. Ko, J. et al. The pathogenesis of systemic sclerosis: the origin of fibrosis and interlink with vasculopathy and autoimmunity. *Int. J. Mol. Sci.* **24**, 14287 (2023).
10. Usategui, A., del Rey, M.J. & Pablos, J.L. Fibroblast abnormalities in the pathogenesis of systemic sclerosis. *Expert Rev. Clin. Immunol.* **7**, 491–498 (2011).
11. Plikus, M.V. et al. Fibroblasts: origins, definitions, and functions in health and disease. *Cell* **184**, 3852–3872 (2021).
12. Kirsch-Volders, M. et al. Micronuclei, inflammation and auto-immune disease. *Mutat. Res. Rev.* **786**, 108335 (2020).
13. Aldrup-Macdonald, M.E. & Sullivan, B.A. The past, present, and future of human centromere genomics. *Genes* **5**, 33–50 (2014).
14. Jeffery, D., Lochhead, M. & Almouzni, G. CENP-A: a histone H3 variant with key roles in centromere architecture in healthy and diseased states. *Results Probl. Cell Differ.* **70**, 221–261 (2022).
15. Logsdon, G.A. et al. Complex genetic variation in nearly complete human genomes. *Nature* **644**, 430–441 (2025).

16. Vona, R. et al. Oxidative stress in the pathogenesis of systemic scleroderma: an overview. *J. Cell. Mol. Med.* **22**, 3308–3314 (2018).

17. Kreuz, S. & Fischle, W. Oxidative stress signaling to chromatin in health and disease. *Epigenomics* **8**, 843–862 (2016).

18. Nassar, R., Thompson, L. & Fouquerel, E. Molecular mechanisms protecting centromeres from self-sabotage and implications for cancer therapy. *NAR Cancer* **5**, zcad019 (2023).

19. McNulty, S.M. & Sullivan, B.A. Alpha satellite DNA biology: finding function in the recesses of the genome. *Chromosome Res.* **26**, 115–138 (2018).

20. Black, E.M. & Giunta, S. Repetitive fragile sites: centromere satellite DNA as a source of genome instability in human diseases. *Genes* **9**, 615 (2018).

21. Fachinetti, D. et al. DNA sequence-specific binding of CENP-B enhances the fidelity of human centromere function. *Dev. Cell* **33**, 314–327 (2015).

22. Krupina, K., Goginashvili, A. & Cleveland, D.W. Causes and consequences of micronuclei. *Curr. Opin. Cell Biol.* **70**, 91–99 (2021).

23. Fenech, M. et al. Micronuclei as biomarkers of DNA damage, aneuploidy, inducers of chromosomal hypermutation and as sources of pro-inflammatory DNA in humans. *Mutat. Res. Rev.* **786**, 108342 (2020).

24. Zhang, C.Z. et al. Chromothripsis from DNA damage in micronuclei. *Nature* **522**, 179–184 (2015).

25. Mackenzie, K.J. et al. cGAS surveillance of micronuclei links genome instability to innate immunity. *Nature* **548**, 461–465 (2017).

26. Harding, S.M. et al. Mitotic progression following DNA damage enables pattern recognition within micronuclei. *Nature* **548**, 466–470 (2017).

27. Gourh, P. et al. HLA and autoantibodies define scleroderma subtypes and risk in African and European Americans and suggest a role for molecular mimicry. *Proc. Natl Acad. Sci. USA* **117**, 552–562 (2020).

28. Furukawa, H. et al. Human leukocyte antigen and systemic sclerosis in Japanese: the sign of the four independent protective alleles. *PLoS ONE* **11**, e0154255 (2016).

29. Dengjel, J. et al. Autophagy promotes MHC class II presentation of peptides from intracellular source proteins. *Proc. Natl Acad. Sci. USA* **102**, 7922–7927 (2005).

30. Münz, C. Antigen processing for MHC class II presentation via autophagy. *Front. Immunol.* **3**, 9 (2012).

31. Gülle, S. et al. Skin and lung fibrosis induced by bleomycin in mice: a systematic review. *Reumatismo* **76**, 22–32 (2024).

32. Chen, J. & Stubbe, J.A. Bleomycin: towards better therapeutics. *Nat. Rev. Cancer* **5**, 102–112 (2005).

33. Murray, V. & Martin, R.F. The sequence specificity of bleomycin-induced DNA damage in intact cells. *J. Biol. Chem.* **260**, 10389–10391 (1985).

34. Hecht, S.M. Bleomycin: new perspectives on the mechanism of action. *J. Nat. Prod.* **63**, 158–168 (2000).

35. Chen, J. et al. Mechanistic studies on bleomycin-mediated DNA damage: multiple binding modes can result in double-stranded DNA cleavage. *Nucleic Acids Res.* **36**, 3781–3790 (2008).

36. Murray, V., Chen, J.K. & Chung, L.H. The interaction of the metallo-glycopeptide anti-tumour drug bleomycin with DNA. *Int. J. Mol. Sci.* **19**, 1372 (2018).

37. Bi, X., Mills, T. & Wu, M. Animal models in systemic sclerosis: an update. *Curr. Opin. Rheumatol.* **35**, 364–370 (2023).

38. Yoshizaki, A. et al. Cell adhesion molecules regulate fibrotic process via Th1/Th2/Th17 balance in a bleomycin-induced scleroderma model. *J. Immunol.* **185**, 2502–2515 (2010).

39. Pawelec, K.M. et al. Prevention of bleomycin-induced lung fibrosis via inhibition of the MRTF/SRF transcription pathway. *Pharmacol. Res. Perspect.* **10**, e01028 (2022).

40. Waseem, M. et al. Crosstalk between oxidative stress, mitochondrial dysfunction, chromosome instability, and the activation of the cGAS-STING/IFN pathway in systemic sclerosis. *Ageing Res. Rev.* **110**, 102812 (2025).

41. Her, J. & Bunting, S.F. How cells ensure correct repair of DNA double-strand breaks. *J. Biol. Chem.* **293**, 10502–10511 (2018).

42. Aymard, F. et al. Transcriptionally active chromatin recruits homologous recombination at DNA double-strand breaks. *Nat. Struct. Mol. Biol.* **21**, 366–374 (2014).

43. Tsouroula, K. et al. Temporal and spatial uncoupling of DSB repair pathways within mammalian heterochromatin. *Mol. Cell* **63**, 293–305 (2016).

44. Zeitlin, S.G. et al. Double-strand DNA breaks recruit the centromeric histone CENP-A. *Proc. Natl Acad. Sci. USA* **106**, 15762–15767 (2009).

45. De Rop, V., Padeganeh, A. & Maddox, P.S. CENP-A: the key player behind centromere identity, propagation, and kinetochore assembly. *Chromosoma* **121**, 527–538 (2012).

46. Saayman, X. et al. Centromeres as universal hotspots of DNA breakage, driving RAD51-mediated recombination during quiescence. *Mol. Cell* **83**, 523–538.e7 (2023).

47. Mitra, S. et al. Rad51–Rad52 mediated maintenance of centromeric chromatin in *Candida albicans*. *PLoS Genet.* **10**, e1004344 (2014).

48. Denais, C.M. et al. Nuclear envelope rupture and repair during cancer cell migration. *Science* **352**, 353–358 (2016).

49. Raab, M. et al. ESCRT III repairs nuclear envelope ruptures during cell migration to limit DNA damage and cell death. *Science* **352**, 359–362 (2016).

50. Kono, Y. et al. Nucleoplasmic lamin C rapidly accumulates at sites of nuclear envelope rupture with BAF and cGAS. *J. Cell Biol.* **221**, e202201024 (2022).

51. Guey, B. et al. BAF restricts cGAS on nuclear DNA to prevent innate immune activation. *Science* **369**, 823–828 (2020).

52. Zhang, J. et al. The role of cGAS–STING signaling in pulmonary fibrosis and its therapeutic potential. *Front. Immunol.* **14**, 1273248 (2023).

53. Wu, X. et al. Ficolin B secreted by alveolar macrophage exosomes exacerbates bleomycin-induced lung injury via ferroptosis through the cGAS–STING pathway. *Cell Death Dis.* **14**, 577 (2023).

54. Savigny, F. et al. Protective role of the nucleic acid sensor STING in pulmonary fibrosis. *Front. Immunol.* **11**, 588799 (2021).

55. Yu, S. et al. Cyclic GMP-AMP synthase expression is enhanced in systemic sclerosis-associated interstitial lung disease and stimulates inflammatory myofibroblast activation. *Eur. Respir. J.* **66**, 2401564 (2025).

56. Benedetti, F. et al. Mycoplasma DnaK expression increases cancer development in vivo upon DNA damage. *Proc. Natl Acad. Sci. USA* **121**, e2320859121 (2024).

57. Contreras-Galindo, R. et al. Rapid molecular assays to study human centromere genomics. *Genome Res.* **27**, 2040–2049 (2017).

58. Wang, B. et al. Artesunate sensitizes ovarian cancer cells to cisplatin by downregulating RAD51. *Cancer Biol. Ther.* **16**, 1548–1556 (2015).

59. Lim, J.W., Kim, H. & Kim, K.H. Expression of Ku70 and Ku80 mediated by NF-κB and cyclooxygenase-2 is related to proliferation of human gastric cancer cells. *J. Biol. Chem.* **277**, 46093–46100 (2002).

Legends to Figures

Fig. 1. Heatmap and qPCR analysis of α-satellite array abundance in fibroblasts and mouse skin after BLM. (A) Representative dorsal skin images of mice after 14 days of saline (vehicle) or BLM injections. Red: vehicle-control skin; yellow: adjacent unaffected skin; blue: fibrotic lesion. (B, C) Quantification of dermal thickness (B) and erythema scores (C) in vehicle and BLM-treated mice (n = 5 per group). (D) Hydroxyproline content measured by colorimetric assay in vehicle-control, unaffected, and fibrotic skin from BLM-treated mice (n = 5 per group). (E) qPCR analysis of mouse centromeric arrays (MaSat, MiSat, Ymin) normalized to 18S. Red lines connect paired unaffected and fibrotic samples. (F, G) Heatmaps showing $\log_2$ fold-change in human α-satellite monomers in CHON-002 fibroblasts after 1-3 h BLM exposure (F) or 3 h BLM followed by 24 h recovery (G). White: loss; blue: gain; grey: stable. DYZ3 was absent in CHON-002 cells as derived from female; TOP3A serves as a non-centromeric reference. Data were mean ± SD. One-way ANOVA: **$p < 0.01$; ***$p < 0.001$; ****$p < 0.0001$; ns, not significant.

Fig. 2. BLM-induced DNA damage at centromere loci. (A) CHON-002 fibroblasts treated with 3.5 or 7.0 μM BLM for 3 h stained for CENP-A (orange), CENP-B (green), γH2AX (red), and DAPI (blue, nuclei). Untreated cells displayed discrete nuclear CENP-A/B foci, whereas BLM-treated cells showed strong γH2AX staining at centromeres. White arrows: micronuclei. (B) Primary fibroblasts from healthy controls and SSc patients stained for CENP-A (green) and γH2AX (purple), with DAPI (blue). Healthy fibroblasts showed minimal γH2AX, whereas SSc fibroblasts exhibited strong γH2AX foci, with persistent centromeric DNA damage.

Fig. 3. Centromeric DNA repair mechanisms after BLM treatment. CHON-002 fibroblasts were treated with 3.5 or 7.0 μM BLM for 3 h followed by 24 h recovery. (A) IF for RAD51 (HR, green), γH2AX (DSBs, orange), and KU70 (NHEJ, purple). Untreated controls showed minimal staining, whereas BLM-treated cells exhibited strong γH2AX foci with prominent RAD51 recruitment at damage sites. White arrows: micronuclei. (B) CENP-A (orange) and RAD51 (green) staining after 3 h BLM exposure showed diffuse nuclear RAD51 without discrete foci, consistent with early-stage HR activation.

Fig. 4. ATM inhibition reduces γH2AX and RAD51 accumulation at centromeres after BLM treatment. CHON-002 fibroblasts were treated with 3.5 or 7.0 μM BLM for 3 h, with or without 1 h pretreatment along with the ATM inhibitor KU-55933 (35 μM). (A) IF for DAPI (blue, nuclei), CENP-A (orange, centromeres), and γH2AX (green, DNA double-strand breaks). BLM induced a dose-dependent increase in γH2AX foci, many colocalizing with CENP-A. ATM inhibition reduced γH2AX accumulation without altering CENP-A localization or intensity. Scale bar, 10 μm. (B) Quantification of mean nuclear γH2AX intensity showing dose-dependent induction by BLM, significantly suppressed by ATM inhibition (n = 50 cells per condition). (C) Quantification of mean nuclear CENP-A intensity showing no significant changes across treatments. (D) IF for DAPI (blue, nuclei) and RAD51 (green, HR). ATM inhibition reduced RAD51 accumulation. Scale bar, 10 μm. (E) Quantification of mean nuclear RAD51 intensity induction by BLM, significantly suppressed by ATM inhibition (n = 50 cells per condition). Data were mean ± SD. One-way ANOVA: *$p < 0.05$; **$p < 0.01$; ***$p < 0.001$; ****$p < 0.0001$; ns, not significant $p > 0.05$.

Fig. 5. BLM induces micronuclei, cytoplasmic centromeric foci, and nuclear envelope rupture. (A) CHON-002 fibroblasts treated with 3.5 or 7.0 µM BLM for 3 h followed by 24 h recovery. IF for CENP-A (orange), CENP-B (green), and DAPI (blue). Controls showed intact nuclei with discrete centromeric foci; BLM induced micronuclei (white arrows) and cytoplasmic centromeric foci (small white arrows). Scale bar, 5 µm. (B-D) Quantification of micronucleated cells (B), micronuclei positive for CENP-A/B (C), and cells with cytoplasmic centromere protein-DNA structures (D). Data were mean ± SD, n = 100 cells per group, three independent experiments. One-way ANOVA: ****$p < 0.0001$; ns, not significant. (E) BANF1 (green) localized to nuclei in controls and redistributed to nuclei and micronuclei after BLM (white arrows), indicating nuclear envelope rupture. DAPI, blue. Scale bar, 5 µm. (F) Quantification of mean BANF1 fluorescence intensity. Data were mean ± SD, n = 10 cells per condition. One-way ANOVA: ****$p < 0.0001$. (G) Primary fibroblasts from healthy controls and SSc patients stained for CENP-A (red), CENP-B (green), and DAPI (blue). Healthy controls showed intact nuclei with discrete centromeric foci; SSc fibroblasts displayed micronuclei and cytoplasmic centromeric foci (white arrows). Scale bar, 10 µm.

Fig. 6. Colocalization of cytoplasmic CENP-B and MHC class II (DRB1) after BLM treatment. CHON-002 fibroblasts were left untreated or treated with 3.5 or 7.0 µM BLM for 3 h followed by 24 h recovery. Cells were stained for CENP-B (orange) and MHC class II (DRB, green); nuclei were counterstained with DAPI (blue). White arrows: cytoplasmic colocalization of CENP-B and MHC II (DRB1). No colocalization was observed in controls. Scale bar, 10 µm.

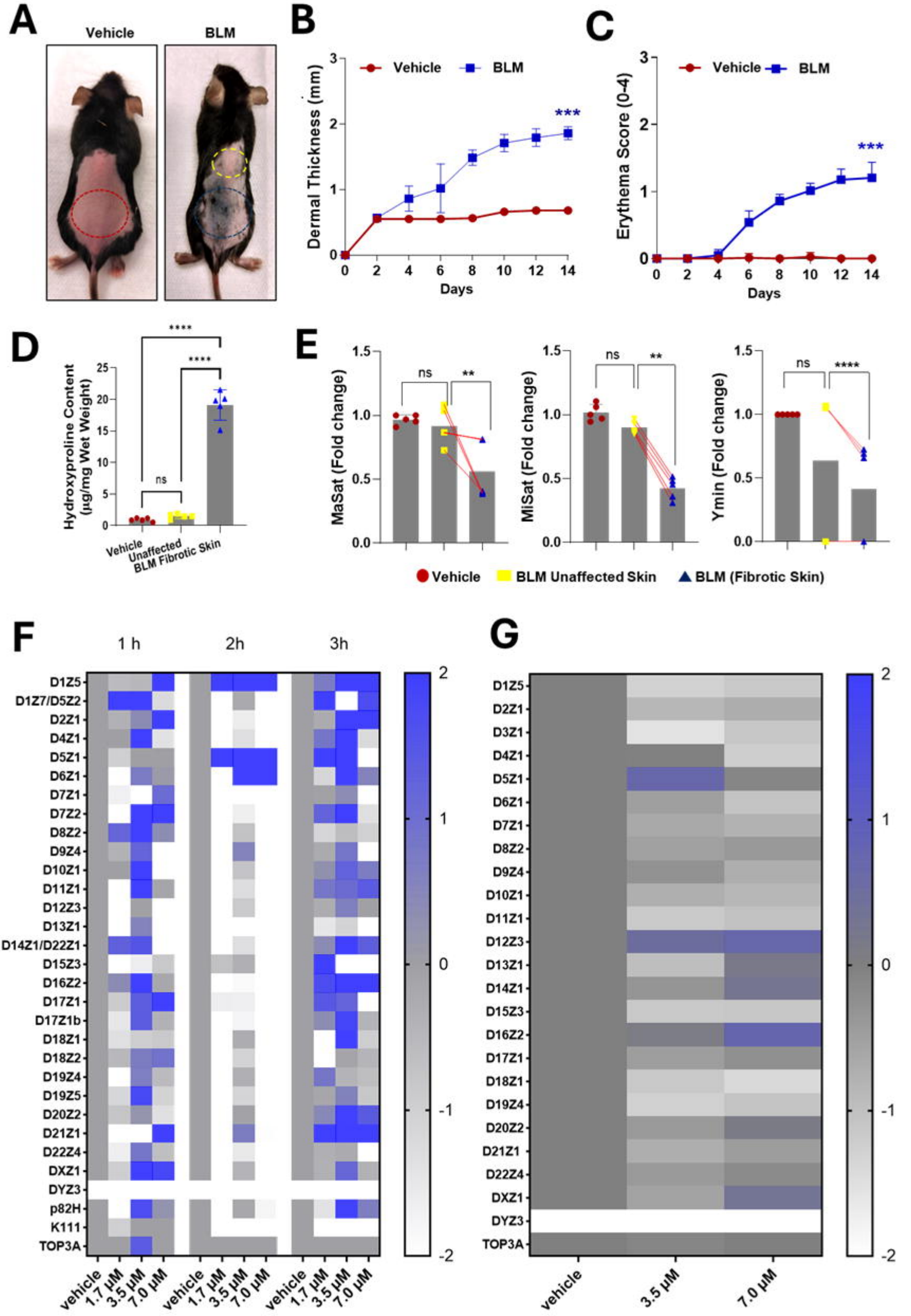
A
Vehicle
BLM
B
Vehicle
BLM
Dermal Thickness (mm)
Days
***
C
Vehicle
BLM
Erythema Score (0-4)
Days
***
D
Hydroxyproline Content (µg/mg Wet Weight)
****
****
ns
Vehicle
Unaffected BLM
Fibrotic Skin
E
MaSat (Fold change)
MiSat (Fold change)
Ymin (Fold change)
ns
**
ns
**
ns
****
Vehicle
BLM Unaffected Skin
BLM (Fibrotic Skin)
F
1 h
2h
3h
D1Z5
D1Z7/D5Z2
D2Z1
D4Z1
D5Z1
D6Z1
D7Z1
D7Z2
D8Z2
D9Z4
D10Z1
D11Z1
D12Z3
D13Z1
D14Z1/D22Z1
D15Z3
D16Z2
D17Z1
D17Z1b
D18Z1
D18Z2
D19Z4
D19Z5
D20Z2
D21Z1
D22Z4
DXZ1
DYZ3
p82H
K111
TOP3A
vehicle
1.7 µM
3.5 µM
7.0 µM
G
D1Z5
D2Z1
D3Z1
D4Z1
D5Z1
D6Z1
D7Z1
D8Z2
D9Z4
D10Z1
D11Z1
D12Z3
D13Z1
D14Z1
D15Z3
D16Z2
D17Z1
D18Z1
D19Z4
D20Z2
D21Z1
D22Z4
DXZ1
DYZ3
TOP3A
vehicle
3.5 µM
7.0 µM

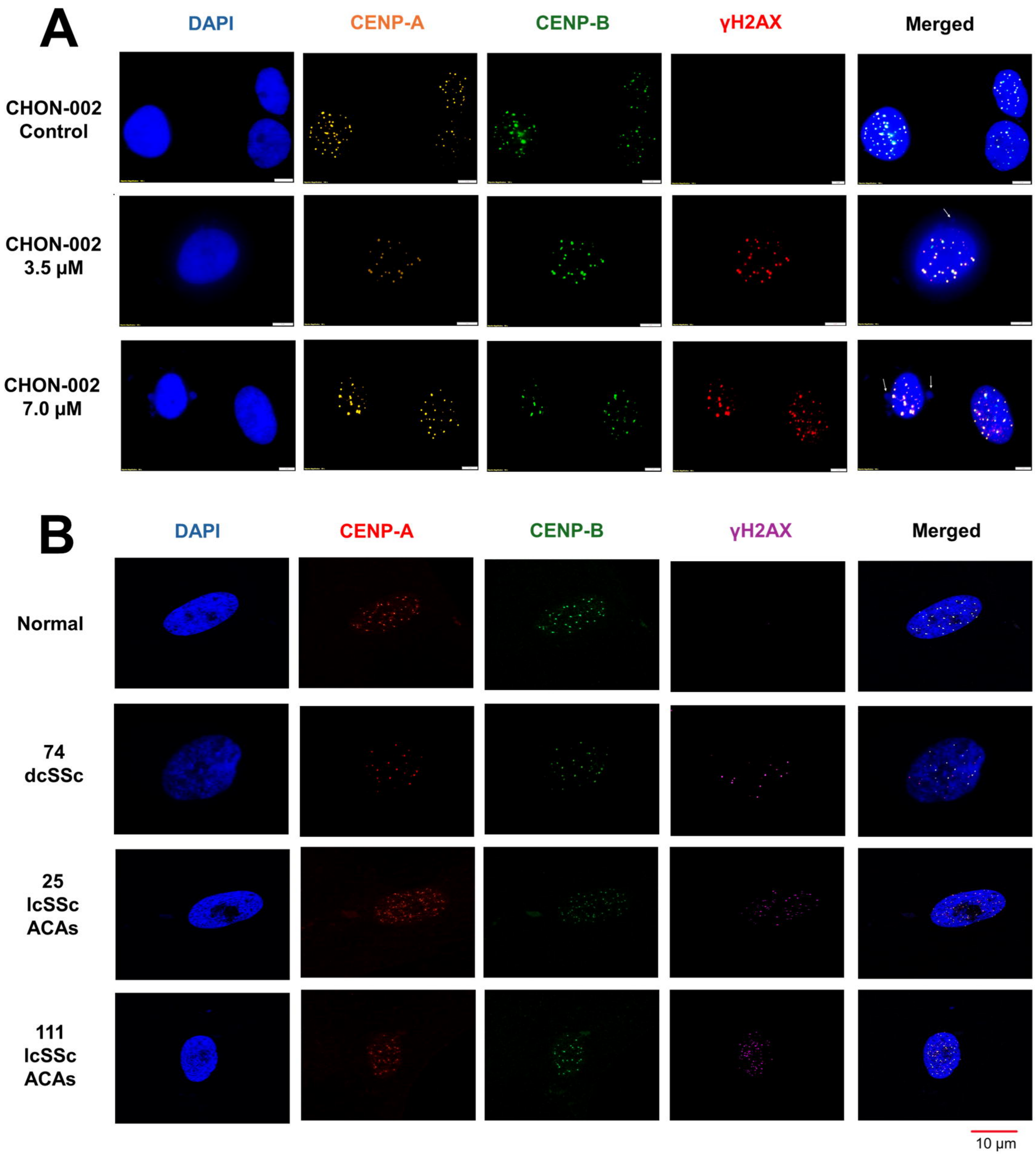
A
DAPI
CENP-A
CENP-B
γH2AX
Merged
CHON-002 Control
CHON-002 3.5 μM
CHON-002 7.0 μM
B
DAPI
CENP-A
CENP-B
γH2AX
Merged
Normal
74 dcSSc
25 lcSSc ACAs
111 lcSSc ACAs
10 μm

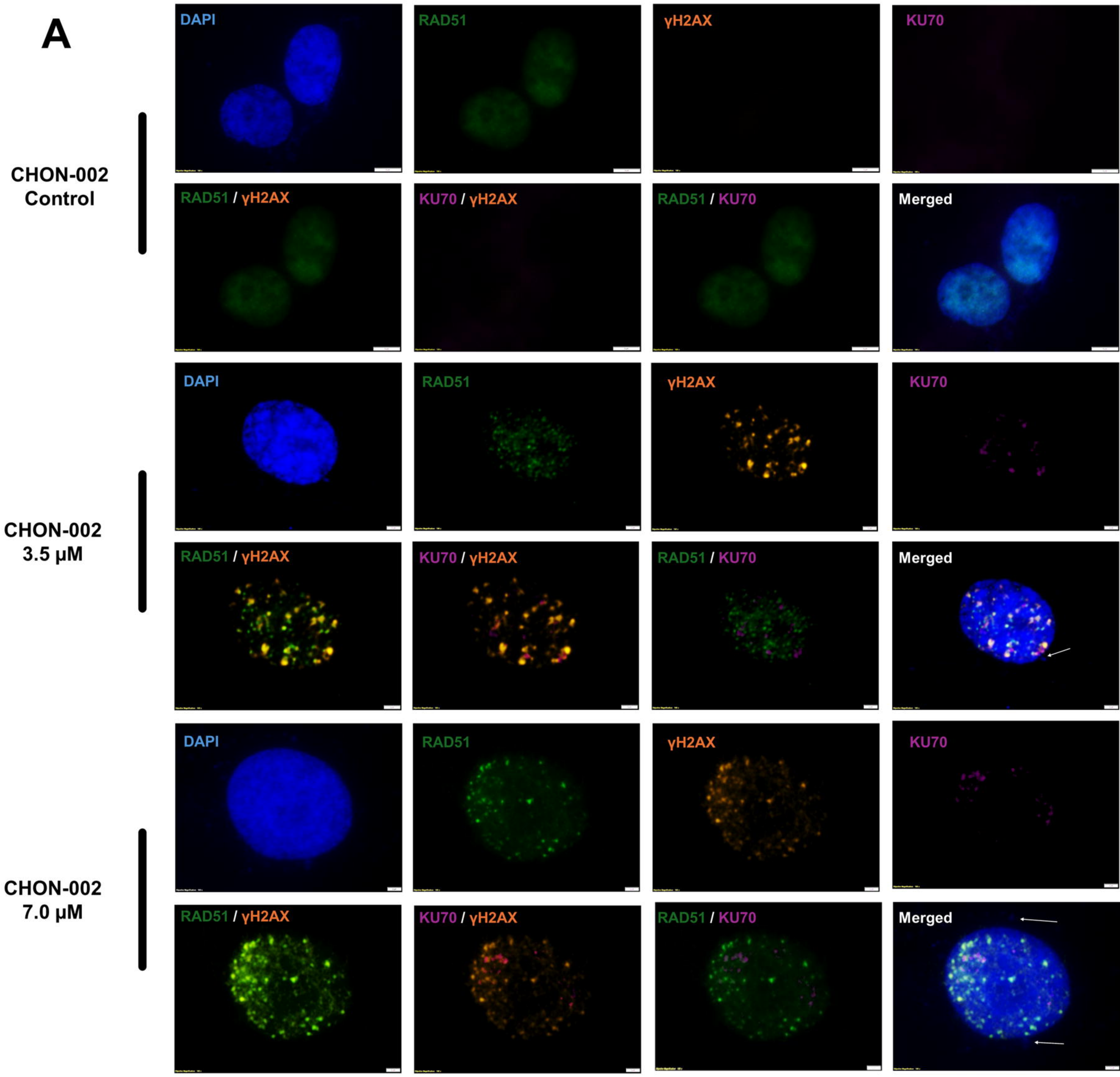
A
CHON-002
Control
DAPI
RAD51
γH2AX
KU70
RAD51 / γH2AX
KU70 / γH2AX
RAD51 / KU70
Merged
CHON-002
3.5 μM
CHON-002
7.0 μM
B
DAPI
CENP-A
RAD51
RAD51/CENP-A
Merged
CHON-002
Control
CHON-002
3.5 μM
CHON-002
7.0 μM

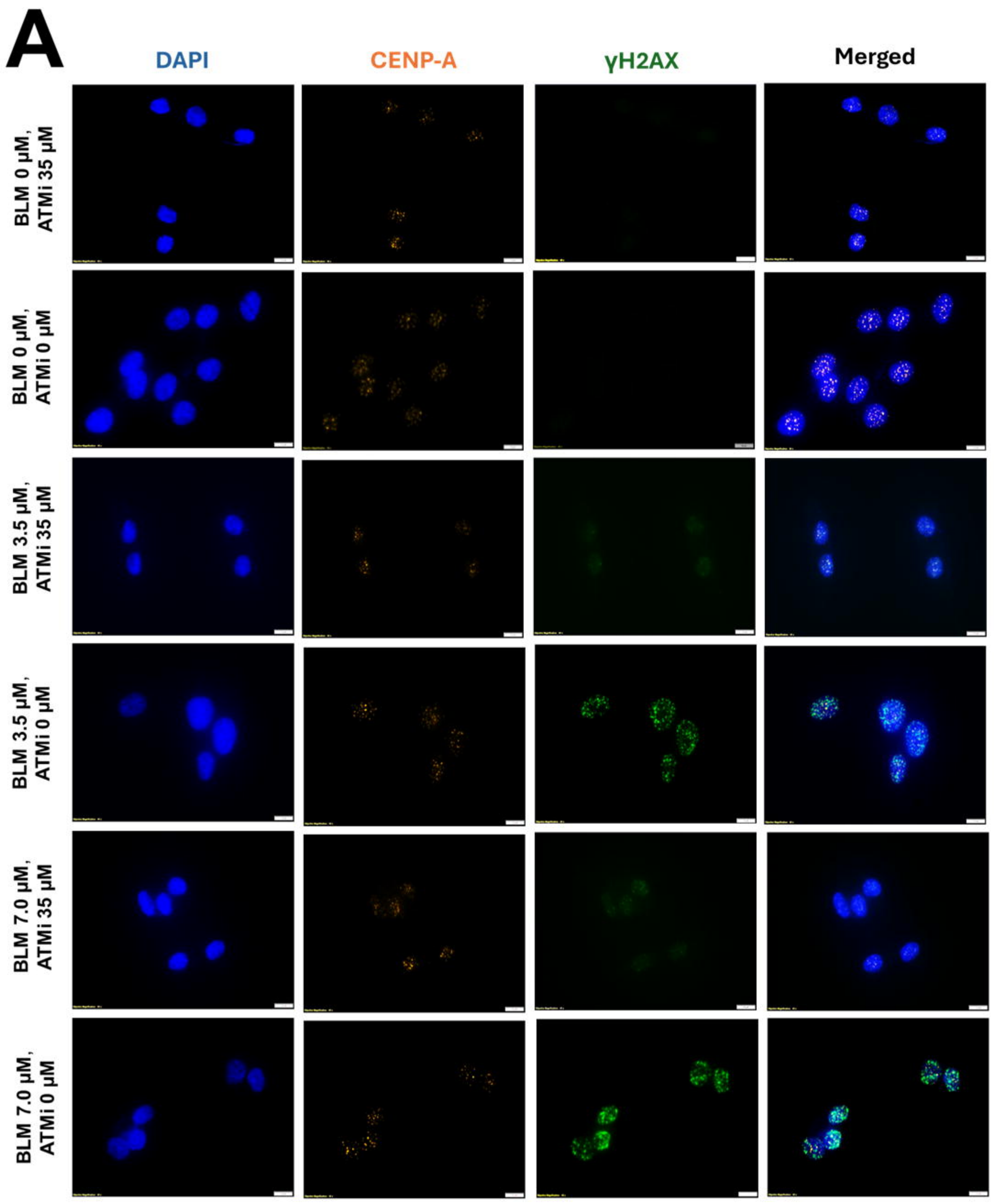
A
DAPI
CENP-A
γH2AX
Merged
BLM 0 μM, ATMi 35 μM
BLM 0 μM, ATMi 0 μM
BLM 3.5 μM, ATMi 35 μM
BLM 3.5 μM, ATMi 0 μM
BLM 7.0 μM, ATMi 35 μM
BLM 7.0 μM, ATMi 0 μM

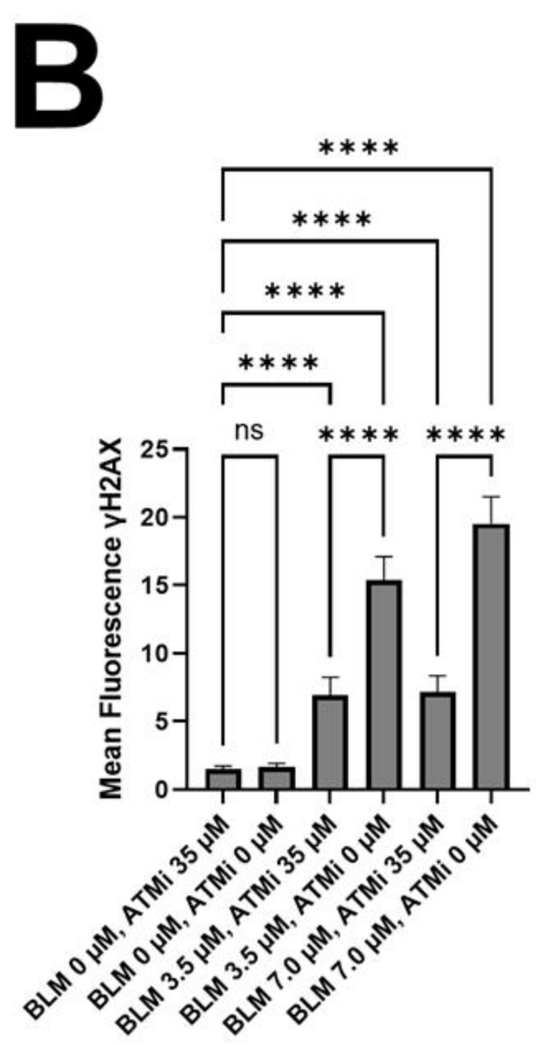
B
Mean Fluorescence γH2AX
0
5
10
15
20
25
ns
****
BLM 0 μM, ATMi 35 μM
BLM 0 μM, ATMi 0 μM
BLM 3.5 μM, ATMi 35 μM
BLM 3.5 μM, ATMi 0 μM
BLM 7.0 μM, ATMi 35 μM
BLM 7.0 μM, ATMi 0 μM

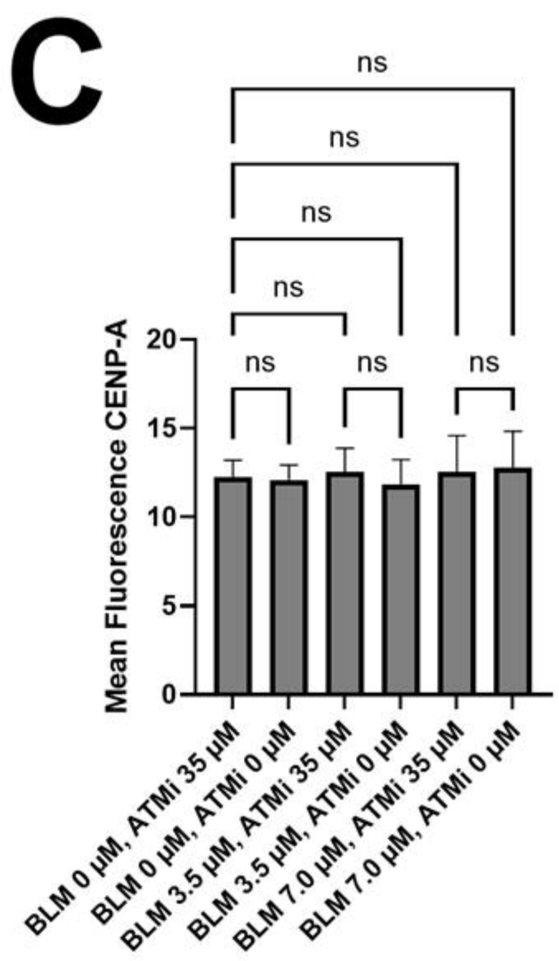
C
Mean Fluorescence CENP-A
0
5
10
15
20
ns
BLM 0 μM, ATMi 35 μM
BLM 0 μM, ATMi 0 μM
BLM 3.5 μM, ATMi 35 μM
BLM 3.5 μM, ATMi 0 μM
BLM 7.0 μM, ATMi 35 μM
BLM 7.0 μM, ATMi 0 μM

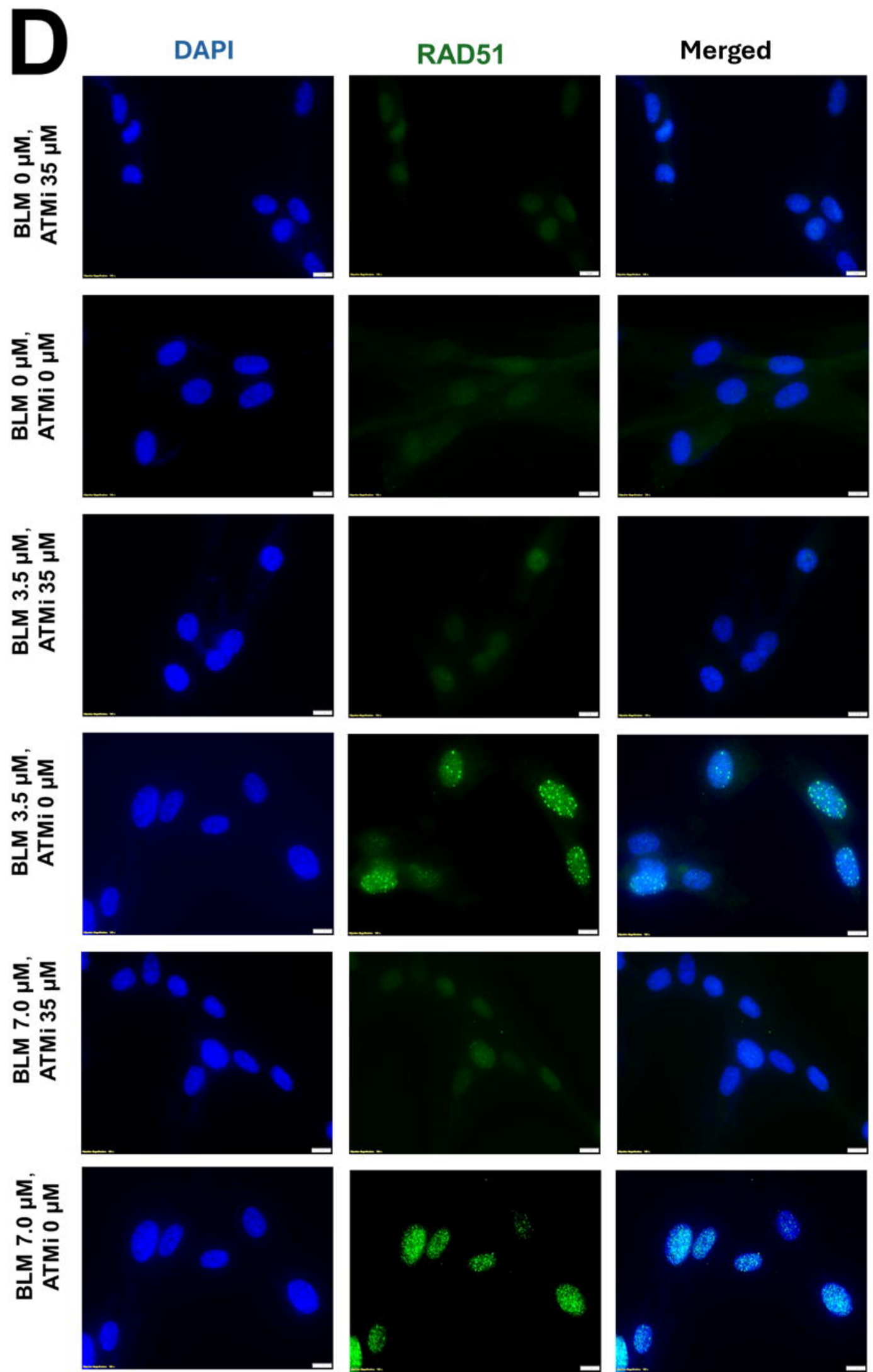
D
DAPI
RAD51
Merged
BLM 0 μM, ATMi 35 μM
BLM 0 μM, ATMi 0 μM
BLM 3.5 μM, ATMi 35 μM
BLM 3.5 μM, ATMi 0 μM
BLM 7.0 μM, ATMi 35 μM
BLM 7.0 μM, ATMi 0 μM

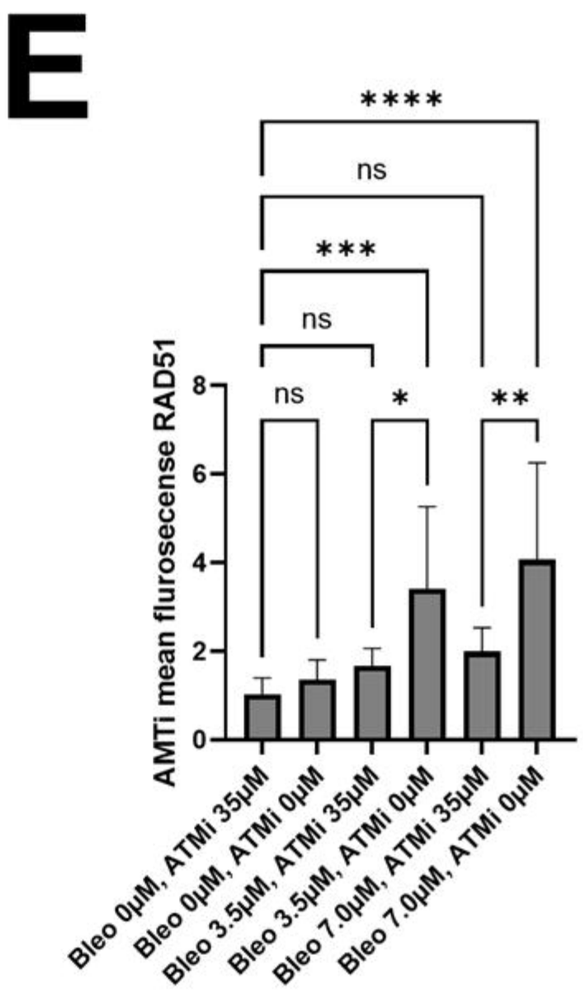
E
AMTi mean flurosecense RAD51
0
2
4
6
8
ns
*
**
***
****
Bleo 0μM, ATMi 35μM
Bleo 0μM, ATMi 0μM
Bleo 3.5μM, ATMi 35μM
Bleo 3.5μM, ATMi 0μM
Bleo 7.0μM, ATMi 35μM
Bleo 7.0μM, ATMi 0μM

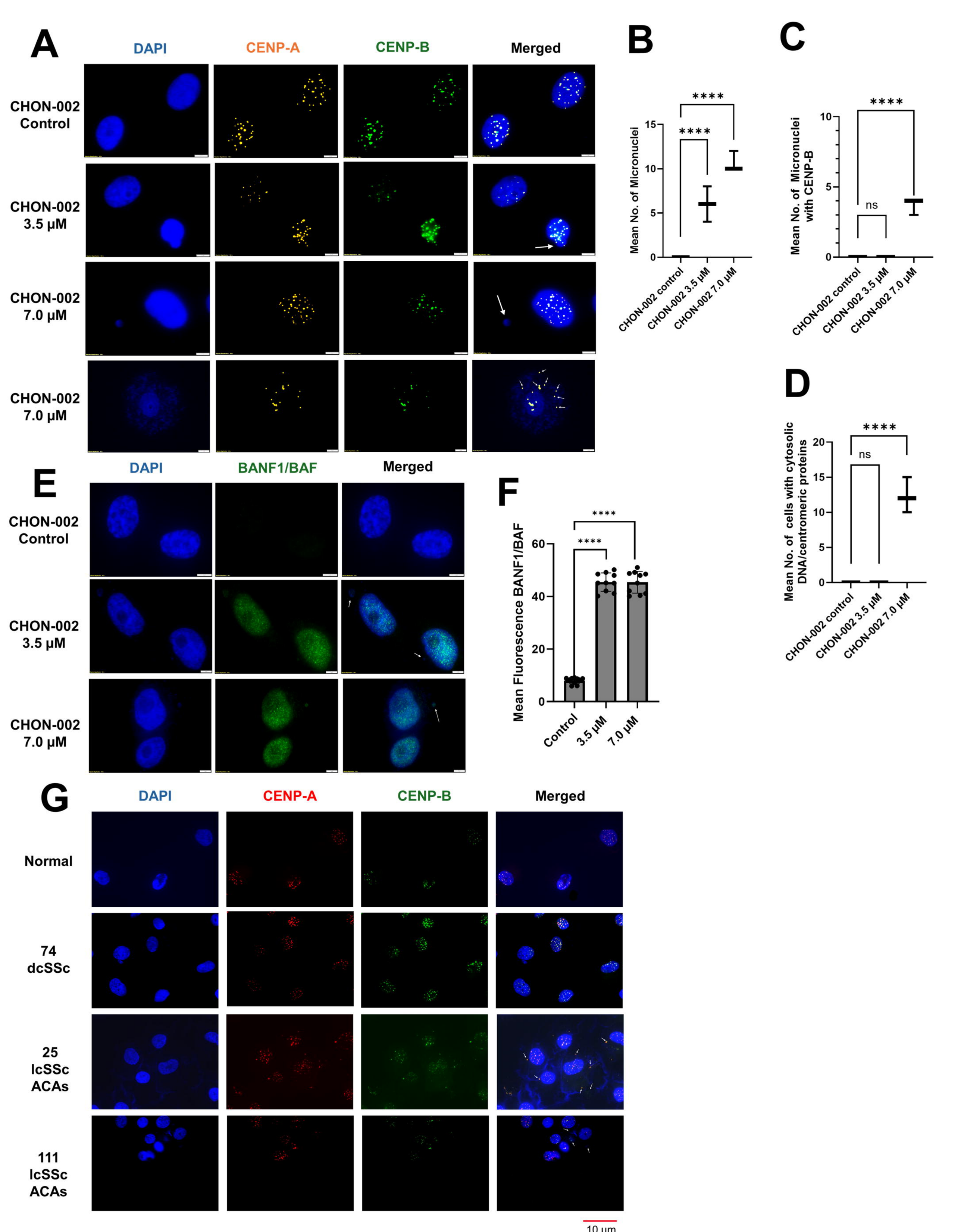
A
DAPI
CENP-A
CENP-B
Merged
CHON-002 Control
CHON-002 3.5 μM
CHON-002 7.0 μM
CHON-002 7.0 μM
B
Mean No. of Micronuclei
****
****
CHON-002 control
CHON-002 3.5 μM
CHON-002 7.0 μM
C
Mean No. of Micronuclei with CENP-B
****
ns
D
Mean No. of cells with cytosolic DNA/centromeric proteins
****
ns
E
DAPI
BANF1/BAF
Merged
CHON-002 Control
CHON-002 3.5 μM
CHON-002 7.0 μM
F
Mean Fluorescence BANF1/BAF
****
****
Control
3.5 μM
7.0 μM
G
DAPI
CENP-A
CENP-B
Merged
Normal
74 dcSSc
25 lcSSc ACAs
111 lcSSc ACAs
10 μm

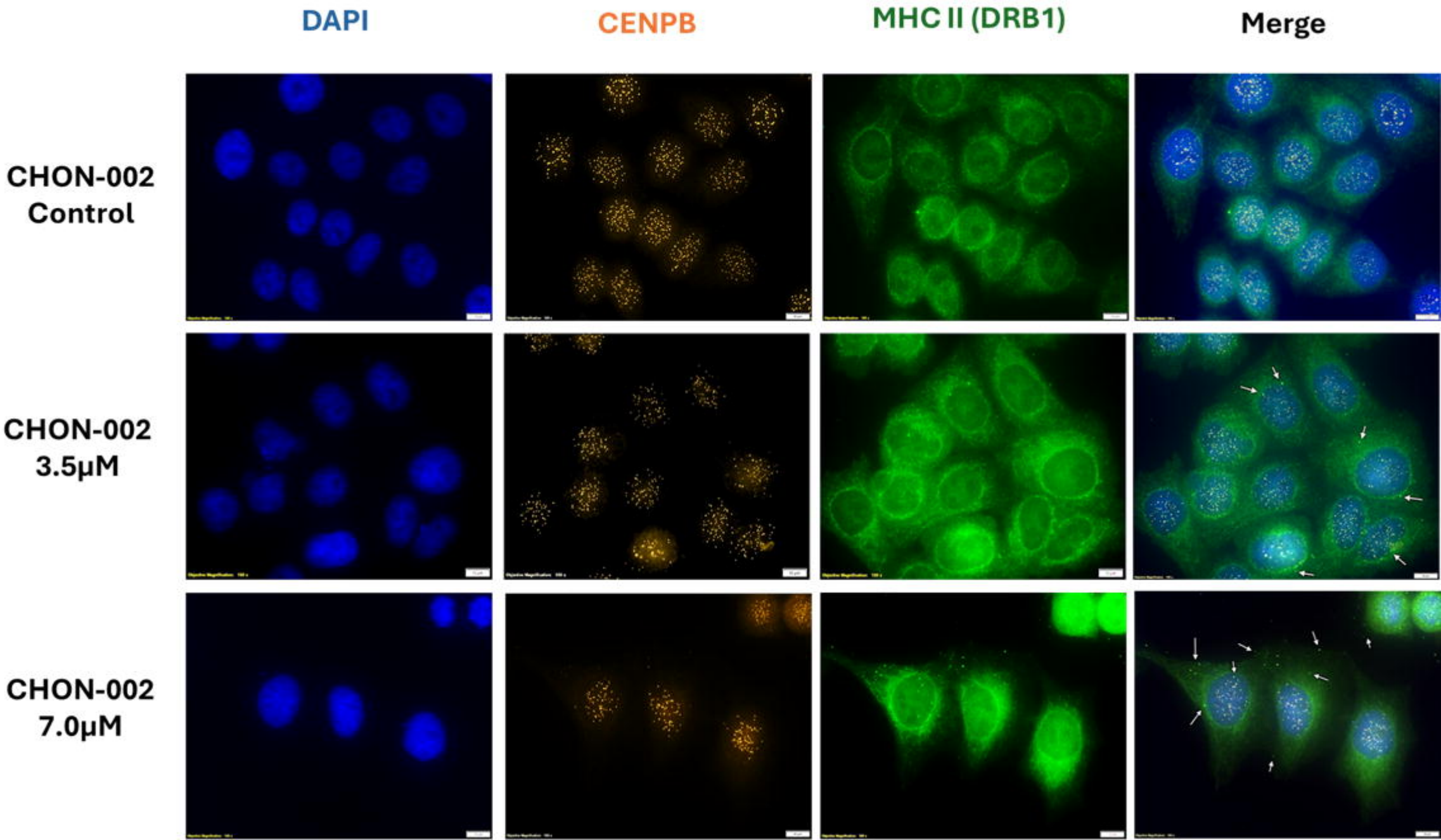
DAPI
CENPB
MHC II (DRB1)
Merge
CHON-002
Control
CHON-002
3.5μM
CHON-002
7.0μM